Journal of the Meteorological Society of Japan

EARLY ONLINE RELEASE

The DOI for this manuscript is
DOI:10.2151/jmsj.2023-013
J-STAGE Advance published date: February 24th, 2023

Analysis of the Factors that Led to Uncertainty of Track Forecast of Typhoon Krosa (2019) by 101-Member Ensemble Forecast Experiments Using NICAM

Masuo NAKANO[1]

Research Institute for Global Change,
Japan Agency for Marine-Earth Science and Technology (JAMSTEC),
Yokohama, Japan

Ying-Wen CHEN

Atmosphere and Ocean Research Institute,
The University of Tokyo, Chiba, Japan

and

Masaki SATOH

Atmosphere and Ocean Research Institute,
The University of Tokyo, Chiba, Japan

February 10, 2023

---

1) Corresponding author: Masuo Nakano, JAMSTEC, 3173-25 Showa-machi, Kanazawa-ku, Yokohama, 236-0001, JAPAN
Email: masuo@jamstec.go.jp
Tel: +81-45-778-5616

Abstract

Typhoon Krosa (2019) formed in the eastern part of the Philippine Sea and ~1400 km east of another typhoon Lekima on 6 August and made landfall in the western part of Japan's mainland on 15 August. The operational global model forecasts, which were initialized just after Krosa's formation, showed a very large uncertainty and totally failed to predict the actual track of Krosa. In this study, we investigated the causes of this large uncertainty through 101-member ensemble forecast experiments by using a 28-km mesh global nonhydrostatic model. The experiments initialized at 1200 UTC 6 August, showed a large uncertainty. An ensemble-based lagged correlation analysis indicated that the western North Pacific Subtropical High (WNPSH) retreated further east in the members with large track forecast errors than in the members with small errors. For the members with a large track forecast error for Krosa, Krosa and Lekima approached each other by 250 km and Krosa moved northward faster than the observation in 36 hours from the initialization time. For the members with a small track forecast error for Krosa, two typhoons approached each other by only 50 km, and the northward moving speed was comparable with that of the observation. The typhoon-center relative composite analysis exhibited that at the initialization time, the members with a large Krosa track forecast error had a larger horizontal size of Krosa and the difference in Krosa's size was kept during the forecast period. This difference in size led to a stronger interaction between the two typhoons and retreatment of the WNPSH, thus resulting in a fast northward moving speed for the members with a large Krosa track error.

Keywords tropical cyclone; track forecast; Fujiwhara effect; forecast bust; western North Pacific subtropical high

1. Introduction

Tropical cyclones (TCs) often cause destructive disasters and threaten human lives and socioeconomics. To mitigate the damages caused by TCs, continuous efforts are needed to improve track forecasts. By 2030, the Japan Meteorological Agency (JMA) aims at reducing the track forecast errors of typhoons on forecast day 3 to less than 100 km, which is approximately half the current forecast error (see Fig 4.1 of JMA 2020). The forecasting of TC tracks has significantly been improved in recent decades. However, the forecasts occasionally experience unusual large errors or uncertainties, which are sometimes called “forecast busts.” Thus, to further improve the track forecasts of TCs, it is necessary to understand what causes such unusual large forecast errors or uncertainties.

The thick color line surrounded by black in each panel of Fig. 1 shows the best track data for Typhoon Krosa (2019). Krosa formed at 0600 UTC 6 August, in the eastern part of the Philippine Sea under the convective envelope associated with the boreal summer intraseasonal oscillation (BSISO; Wang and Rui 1990; Wang and Xie 1997; Kikuchi 2021). Afterward, by 8 August, it moved northwestward, and by 11 August, it slowed down and made a complex trajectory. Subsequently, it moved northwest/north-northwest again and, on 15 August, made landfall on the Hiroshima prefecture, the western part of the mainland of Japan. It should be noted that at the formation time of Krosa, another typhoon, Lekima, was located at ~1400 km west of Krosa. Lekima moved northwestward and made landfall on the central part of the mainland of China on 9 August.

Fig. 1

The operational models initialized at 1200 UTC 6 August, showed a very large uncertainty in forecasting Krosa's track (Figs. 1a, 1e, and 1i). For example, the European Centre for Medium-Range Weather Forecasts (ECMWF) and JMA models barely captured the observed Krosa's track within the uncertainty range. However, the spread was very large; the westernmost track would hit Korea, and the easternmost track would go through the oceanic area east of Japan without making landfall (Figs. 1a and 1e). The National Centers for Environmental Prediction (NCEP) model showed a small uncertainty; however, it totally failed to predict the actual track of Krosa; all members predicted that Krosa would go through to the east of Japan without making landfall (Fig 1i). For the later model initialization time, the uncertainty of Krosa's track forecast decreased, and the forecasts of the three models converged to the observed track in the experiments initialized at 1200 UTC 9 August (Figs 1d, 1h, and 1i).

In the western North Pacific (WNP) region, it is well known that the WNP subtropical high (WNPSH) strongly modulates TC tracks in various time scales. TC tracks are modulated by the convective activity in the tropics since it affects the westward extension of WNPSH (Lu and Dong 2001). Nakazawa and Rajendran (2007) found that the seasonal number of TCs approaching Japan or making landfall on it is strongly modulated by the presence of an anticyclonic anomalous circulation east of the Philippines due to the shifting of the WNPSH westward, resulting in a lower-than-normal TC frequency over Japan. Choi et al. (2010) showed that the Pacific–Japan pattern (Nitta 1987) changes the TC activity in WNP. In addition, Nakano et al. (2021) showed that the suppressed and enhanced convection associated with BSISO affects TC tracks, and this impact is well reproduced by the ECMWF model. Camp et al.

(2019) showed the potential of TC landfall seasonal forecasts by using WNPSH indices predicted by UK MetOffice's global seasonal forecast system in June–August. It is worth noting that a TC creates anticyclonic anomaly northeast of its location due to the Rossby response to its convective heating (Kawamura and Ogasawara 2006), resulting in WNPSH enhancement.

In the cases when two or more TCs closely coexist, they interact with each other (a.k.a. "Fujiwhara effect"; Fujiwhara 1921, 1923). Brand (1970) showed that the interaction characteristics depend on the separation distance between such TCs; rotating cyclonically within each other when the separation distance is less than 750 NM (~1390 km) and attracting each other when the separation distance is less than 400 NM (~740 km). Peng and Reynolds (2005) showed that an interaction can occur even when the separation distance is 1861 km. Moreover, Brand (1970) mentioned that the track forecast errors for TCs the Fujiwhara effect taking place were larger than average in the 1960's. The forecast bust cases associated with such storms can still be seen in state-of-the-art numerical weather prediction systems (e.g., Choi et al. 2017).

The ensemble-based sensitivity analysis (Ancell and Hakim 2007; Torn and Hakim 2008) and clustering the ensemble members by using a ranking of a metric or the characteristics of predicted TC tracks are used to diagnose the main cause of forecast bust. Nakashita and Enomoto (2021) performed an ensemble sensitivity analysis for Typhoon Hagibis (2019) and found that the ensemble members with large track errors have an initial perturbation to weaken the ridge of WNPSH. Magnusson et al. (2014) explored the main causes of the uncertainties in the forecasting of Hurricane Sandy (2012), which made landfall on the eastern coast of the US from the Atlantic, by grouping the

ensemble members into landfall members and moving to the east members and suggested that weaker extension of the subtropical ridge resulted in eastward track.

In this study, we investigated the main causes of the large uncertainty in Krosa's track forecasting through 101-member ensemble forecast experiments by using a global nonhydrostatic model. The rest of this paper is organized as follows. Section 2 describes the experimental setup of the ensemble forecast experiments. Section 3 introduces the data utilized in this study except for the model experimental data and explains the analysis methods. Section 4 shows the results of the experiments, a discussion, and a comparison of the operational model data. Section 5 presents the summary and conclusions of this study.

2. Model Experiment

The model used in this study is a 28-km mesh Nonhydrostatic ICosahedral Atmospheric Model (NICAM [version NICAM.18]; Satoh et al. 2014; Kodama et al. 2021). The number of vertical layers was set to 38, and the model top was located at 37 km. The moist convection was explicitly calculated using a single-moment cloud microphysics scheme (Roh and Satoh 2014) without any cumulus parameterization. The atmospheric initial condition was provided by an operational weather analysis system called NICAM-LETKF JAXA Research Analysis (NEXRA, https://www.eorc.jaxa.jp/theme/NEXRA/index_e.htm, Kotsuki et al. 2019). NEXRA's core data assimilation system is NICAM-LETKF (Terasaki and Miyoshi 2017; Kotsuki et al. 2017), and it combines the ensemble

159 simulation obtained by NICAM and the in situ/satellite observations by LETKF
160 (local ensemble transformed Kalman filter, Hunt et al. 2017). Note that neither
161 TC position and intensity analysis data (so-called TCVITAL) nor Synthetic
162 Tropical Cyclone Bogus Reports (SYNDAT) are assimilated for NEXRA
163 production. The ensemble size and horizontal resolution of NEXRA were 100
164 and 112 km, respectively. We used all the ensemble analysis members (100)
165 and their mean for the model initialization. Thus, there were 101 members in
166 total. SST was predicted by a slab ocean model with a constant depth of 15 m.
167 Moreover, SST was nudged toward the initial values with an e-folding time of 7
168 days. The initial value of SST (1°×1° horizontal resolution) was obtained from
169 the Global Data Assimilation System of NCEP. The SST data was also used in
170 NEXRA's data assimilation cycle. The model simulations were initialized at 1200
171 UTC from the 6th to the 9th of August and integrated for 10 days to examine
172 whether the model can reproduce a large uncertainty.
173

174 **3. Data and Method**

175 The best track data of the Regional Specialized Meteorological Center (RSMC;
176 Tokyo) was used as observational data of the TC location and minimum sea
177 level pressure. The operational ensemble forecasts of ECMWF, JMA, and
178 NCEP (see Table 1), which were taken from the International Grand Global
179 Ensemble archive (TIGGE; Bougeault et al. 2010; Swinbank et al. 2016), were
180 used for the comparison with the NICAM forecasts and discussion. As the
181 resolution of archived data varies by the operational center and is the coarsest
182 for JMA data, the other center's data was regridded to the same resolution, 1.25

Table 1

183 × 1.25 deg.

184 As analyzed by Nakano et al. (2017), the TCs in the model were tracked by
185 searching the sea level pressure (SLP) minimum nearest to the observed TC
186 center at the initial time and by connecting the nearest SLP minimum along with
187 the forecast period. Before searching the SLP minimum, the SLP field was
188 smoothed 100 times using a Gaussian (1-2-1) filter to avoid tracking a meso-
189 vortex embedded in the typhoon scale vortex (e.g., Nolan et al. 2001) or a
190 spurious minimum, which can be caused by numerical noise (e.g., so-called grid
191 storm). To define the TC center in NEXRA, the geopotential height at 925 hPa
192 was used instead of the SLP because the SLP for each ensemble member was
193 not available.

194 Because JMA issues 5-day TC track forecast, reducing TC track error, the
195 distance between the TC center positions analyzed in the best track data and
196 forecasted by the model, 5 days later of Krosa's genesis is of interest. To
197 examine the sensitivity of Krosa's track forecast, we performed an ensemble-
198 based lagged correlation analysis and a best-worst comparison. The lagged
199 correlation is formulated with track forecast error at 1200 UTC 11 August 2019,
200 about 5 days later from Krosa's genesis (*J)* and the atmospheric fields (*F)* of
201 interest at any time *t* including initial time as

203 $$Corr(x,y,t) = \frac{cov(J, F(x,y,t))}{\sigma(J)\sigma(F(x,y,t))}$$

202

204 Where *cov* is the covariance between two arguments and σ is the standard
205 deviation. In the best-worst comparison, the best 20% and worst 20% ensemble
206 members in terms of the TC track forecast errors for Krosa at 1200 UTC 11

August 2019 were selected. Then, the difference in the ensemble mean of each group was analyzed.

4. Results and Discussion

4.1 General results

Figure 2 shows the predicted Krosa's track in all the ensemble simulations by NICAM. The simulations initialized at 1200 UTC 6 August (Fig. 2a) represent a large uncertainty in Krosa's track; the westernmost track makes landfall on the Korean Peninsula, and the easternmost track passes through the east of the Japanese Islands without making landfall. The uncertainty decreases with a later model initialization date with a slight eastward bias. The simulations initialized at 0000 UTC 9 August (Fig. 2d) reasonably capture the observed Krosa's track. This uncertainty reduction in the latter model initialization date was also seen in the operational ensemble forecast system (Fig. 1). Thus, the main uncertainty cause can be analyzed in detail using the NICAM simulation data initialized at 1200 UTC 6 August.

Fig. 2

TC tracks are generally affected by vertically averaged flows, which are also called steering flows. The steering flow can be roughly represented as a geostrophic flow at 500 hPa, although the depth of steering flow is sensitive to the TC intensity (Velden and Leslie 1991). Therefore, the ensemble-based sensitivity analysis was performed using the geopotential height at 500 hPa (Z500) and Krosa's track forecast error at 1200 UTC 11 August (Fig. 3). There was no high sensitivity region in NEXRA, which was used at the model initialization time (Fig. 3a). At 0000 UTC 7 August (Fig. 3b), the lagged

Fig. 3

231 correlation between Z500 and Krosa's track forecast error on 11 August
232 became low between the two typhoons of Krosa and Lekima, and the region
233 extended toward the Japanese Islands along with the forecast time (Figs 3c
234 and 3d). This result indicates that Z500 is relatively low (high) in the member
235 with a large (small) Krosa track forecast error. In addition to the negative
236 correlation region, two positive correlation regions appeared in the northwest
237 of Lekima's center and southeast of Krosa's center. This indicates that Z500 is
238 relatively high (low) in the members with large (small) track forecast errors for
239 Krosa. These results suggest that Krosa's track forecast is sensitive to the
240 distance between the two typhoons.

241 To examine the mechanism behind this forecast sensitivity, the best 20% and
242 worst 20% members (20 members for both) in terms of Krosa's track forecast
243 errors at 1200 UTC 11 August were selected and compared with each other.
244 The best (worst) members had a forecast track error of less than 600 km
245 (more than 1700 km) at 1200 UTC 11 August. Figure 4 represents Krosa and
246 Lekima's track forecasts for the best, worst, and other members. The best
247 members (Fig. 4a) predicted a stall in Krosa from the 9th to the 11th of August
248 and subsequent northwestward or north-northwestward track. The worst
249 members (Fig. 4b) predicted a fast northward movement of Krosa two days
250 after the model initialization time and movement toward the east of Japan. For
251 Lekima's track forecast, the best members (Fig. 4c) well captured the observed
252 track. However, the worst members (Fig. 4d) predicted the recurvature of
253 Lekima toward Japan. These results suggest that the main cause of the track
254 forecast errors of both typhoons is the same.

Fig. 4

255 Figure 5 shows that 5860-m (approximating the edge of WNPSH) and 5760-

Fig. 5

256 m (indicating Krosa and Lekima) contours simulated by the best and worst
257 members. Although there was a little difference between the ensemble means
258 of the best and worst members at 0000 UTC 7 August (Fig 5a), the differences
259 became apparent afterward. With the worst members at 0000 UTC 8 August,
260 Krosa was predicted northwest of the Krosa predicted with the best members
261 and Lekima shifted slightly east of that predicted with the best members (Fig
262 5b). Thus, the distance between the two typhoons was small with the worst
263 members. In addition, the WNPSH over Japan retreated further east with the
264 worst members. These differences became larger at 0000UTC 9 August (Fig
265 5c). These results are consistent with those of the ensemble-based sensitivity
266 analysis (Fig. 3).

267 Figure 6a shows the ensemble mean of six-hourly positions of the two
268 typhoons predicted with the best and worst members. Whereas Krosa moved
269 northward fast with the worst members, the northward migration with the best
270 members was slow and was almost stalled after forecast time of 48 hours (FT =
271 48 h). With the best members, Lekima moved northwestward faster than with
272 the worst members. In addition, with the worst members, the recurvature of
273 Lekima was predicted at approximately FT = 48 h. Krosa's track forecast error
274 (Fig. 6b) with the worst members rapidly grew after FT = 18 h and became
275 greater than 1000 km at FT = 66. However, Krosa's track forecast error was not
276 so large (~220 km) with the best members at FT = 72 h. It is worth noting that
277 the position error at FT = 1 h is slightly larger with the worst members than that
278 with the best members. Lekima's track forecast error was almost the same
279 among the best and worst members at FT = 6 h. However, the error with the
280 worst members became greater in the latter forecast time and rapidly grew

Fig. 6

281 starting from FT = 48 h. The distance between the two typhoons (Fig. 6c) with
282 the worst members was 1400 km at FT = 1 h. Afterward, it decreased to 1150
283 km by FT = 36 h and then increased at the later forecast time. The best
284 members had little distance changes until FT = 24 h. However, the distance
285 rapidly increased at a later forecast time. Assuming that both groups represent
286 the same vortex structure of the typhoons, the interaction between both
287 typhoons could occur easily when the distance between the two typhoons was
288 close. Thus, the interaction between the two typhoons would be stronger with
289 the worst members than with the best members. The predicted Krosa's central
290 minimum pressure (Fig. 6d) is deeper than the best track data from the initial
291 time to FT = 30 h with both members. The model represented Lekima to be
292 shallower in both members than analyzed with the best track. Thus, the bias in
293 the central pressure for both typhoons seems not to be related to the track
294 forecast error.

295 These results suggest that the degree of interaction between the two
296 typhoons and the retreatment of WNPSH affected the uncertainty of Krosa's
297 track forecast. These two points are discussed in the following subsections.

298

299 *4.2 Why did the strong interaction occur in the worst members?*

300 Figure 7 shows the locations of the typhoons' centers for both the best and
301 worst 20 members and the ensemble mean SLP distributions. The existence
302 frequency of the typhoons' centers in the east-west and south-north directions
303 are also shown. At FT = 1 h (Fig. 7a), the low SLP area associated with Krosa
304 for the worst members located slightly to the west of that of the best members.
305 Corresponding to this westward shift, the existence frequency of Krosa's center

Fig. 7

306 in the east (west) of 142°E was less (more) with the worst members than with
307 the best members, whereas the frequency was almost the same in the south-
308 north direction for both members. It is worth noting that simulated Krosa's
309 centers are biased to the northwest of the best track even in the best members.
310 This bias is originated from analysis fields in NEXRA (not shown). It suggests
311 that there is room to improve analysis fields further. These points are discussed
312 later. At FT = 12 h (Fig. 7b), the SLP distributions of Krosa with the worst
313 members shifted to the northwest of those with the best members. The
314 analyzed center location was well captured by the simulated existence
315 frequency with the best members. However, it is out of range of the simulated
316 existence frequency by the worst members, especially in the east-west
317 direction. Nevertheless, the SLP distribution and existence frequency of the
318 typhoon center for Lekima were almost the same with both the best and worst
319 members (Figs. 7c–d). These results suggest that differences in the TC
320 structure or environments of Krosa may lead to the strong interaction between
321 Krosa and Lekima in the worst members.

322 To examine the differences in the typhoon structure, a composite analysis
323 relative to the typhoon's center was performed. Figure 8 shows the composite
324 around Krosa's center in NEXRA at the model initialization time (1200 UTC 6
325 August) for the best and worst members. The low geopotential height at 925
326 hPa (Z925) area near the western edge represents the eastern part of Lekima.
327 The 680-m contour of Z925 was separated in the composite of the best member
328 (Fig. 8a); however, it was connected to Lekima in the composite of the worst
329 members (Fig. 8b). The differences in Z925 (Fig. 8c) indicate that there was an
330 anticyclonic anomaly north of Krosa's center with the best members in

Fig. 8

331 comparison with the worst members. The lagged correlation analysis (Fig. 8d)
332 showed consistent results; Z925 is lower (higher) when the track forecast error
333 at 1200 UTC 11 August is larger (smaller). The 10-m wind speed was larger at
334 the east of Krosa's center with both the best and worst members than at the
335 west (Figs. 8e and 8f). The small wind speed was induced by a confluence of
336 the northerly wind by Krosa and the southerly wind by Lekima. The difference
337 between the best and worst members indicates the weak wind speed anomaly
338 in the eastern semicircle (Fig. 8g). The lagged correlation analysis (Fig. 8h)
339 showed the consistent results; the 10-m wind speed is higher (lower) when the
340 track forecast error at 1200 UTC 11 August is larger (smaller). These results
341 indicate that the Krosa in the worst members had a larger circulation than that in
342 the best members.

343 Although apparent differences in the vortex structure of Krosa could be found
344 between the best and worst members, a very little difference in Lekima's
345 structure was found (Fig.9). The anomaly of 10 degrees east of Lekima's center
346 can be related to the differences in Krosa's position and size. The Z925 was
347 higher in the best members (Fig. 9c). This result is consistent with the lagged
348 correlation analysis (Fig. 9d). The confluence region of Krosa's northerly and
349 Lekima's southerly was shifted to the west more with the worst members than
350 with the best members. The lagged correlation analysis indicates this feature by
351 the dipole structure east of the TC center (Fig. 9h), whereas the difference
352 between the best and worst members showed negative anomaly only there
353 (Fig. 9g).

Fig. 9

354 How the difference in the initial conditions affects the forecast? Figure 10
355 shows that SLP at 1800 UTC 6 August (FT = 6 h) in the east and west of

Fig. 10

356 Krosa's center is lower (Fig. 10a) and 10-m wind speed of the outer region,
357 especially from east to south, is larger (Fig. 10b) in the members with larger
358 Krosa's track forecast error at 1200 UTC 11 August. These results indicate that
359 Krosa's size is larger in the members with larger track error. The negative
360 correlation for SLP (Fig. 10c) and the positive correlation for 10 m wind speed
361 (Fig. 10d) became stronger and surrounded the storm center at 1200 UTC 7
362 August. These results suggest that Krosa's structure at the initial condition
363 affected the vortex structure in the model forecast. The initial vortex structure,
364 which was larger in size with the worst members, led to active convection in the
365 outer region. Thus, the larger vortex structure and stronger interaction with
366 Lekima with the worst members were withheld.
367
368 *4.3 Why did a difference in WNPSH occur?*
369 The variation of the WNPSH should be influenced by whether the mass
370 concentration/dissipation had occurred near the Japanese Islands. Figures 11
371 and 12 show the divergence and the geopotential height for the best and worst
372 members at 200 and 925 hPa, respectively. In the best members (a–c of Figs.
373 11–12), the trough at 200 hPa existed to the northeast of Krosa. Therefore,
374 Krosa was embedded in northerly wind environment at 200hPa induced by the
375 trough and anticyclonic circulation above Lekima existing to the west of Krosa.
376 At 925 hPa, the WNPSH existed to the east and north of Krosa. Thus, Krosa
377 was embedded in southerly wind environment caused by the WNPSH and
378 cyclonic circulation of Lekima. Thus, Krosa was embedded in, generally,
379 northerly vertical wind shear environment (Fig. 13a). Recall that the convective
380 activity enhanced downshear/downshear left quadrant (Corbosiero and Molinari

Fig. 11

Fig. 12

Fig. 13

381 2002; Ueno 2007), Krosa's convection, thus convergence at 925 hPa and the
382 divergence at 200 hPa, biased to the south to southeast of the storm center.
383 The best members well reproduced these features (a–c of Figs 11–12). In the
384 worst members (d–f of Figs 11–12), convergence at 925 hPa and the
385 divergence at 200 hPa, biased to the south quadrant at 0000 UTC 7 August and
386 these shifted to the east quadrant two days later. It is attributed to changes in
387 direction of vertical wind shear, from northerly to westerly (Fig. 13b),
388 accompanied by northward movement of Krosa and presumably begin to be
389 affected by the jet stream (Ito and Ichikawa 2021). This eastward-biased
390 divergence at 200 hPa in the worst members may resulted in eastward-biased
391 difference in Z925 (Fig. 12i) leading to the WNPSH retreatment.

392 It should be noted that the area of divergence at 200 hPa is larger in the
393 worst members than that in the best members. This larger area of divergence
394 near the tropopause may cause wider area pressure decrease in the lower-
395 levels. In fact, Fig. 12i shows that larger area of positive Z925 anomaly (best
396 member – worst member). This supports that decreases in geopotential height
397 in wider area occurred in the worst members. Fig 14 shows time series of the
398 lagged correlation between divergence within 6 degrees (inner area) and 6–9.5
399 degrees away (outer area) from the Krosa's center and TC track forecast error
400 at 1200 UTC 11 August. In the inner area (Fig. 14a), lower-level convergence
401 and upper-level divergence are large (small) when the Krosa's track forecast
402 error is small (large) after 1200 UTC 7 August (FT = 24 h). In the outer area,
403 lower level convergence and upper level divergence are small (large) when the
404 Krosa's track forecast error is small (large) after 1200 UTC 7 August (FT = 24
405 h). Sun et al. (2015) demonstrated that significant 500 hPa height decrease

Fig. 14

406 leading to the breaking of WNPSH occurred after 2–3 days integration when the
407 initial storm size is large. Our results also suggest that the larger storm size in
408 the worst members leads to retreat of the WNPSH.
409
410 *4.4 Did the same situation happen in the operational models?*
411 The readers may wonder whether the proposed mechanism worked in the
412 operational ensemble forecast systems. The operational centers' forecasts were
413 grouped into best and worst and then compared to speculate this point.
414 However, analyzing the mechanism in detail using operational model data is
415 beyond the aim of this paper, as the archived data resolution is much coarser
416 than the actual model resolution except for ECMWF (Table 1). Figure 15 shows
417 the spaghetti diagram of Z500 for the best and worst members for each
418 operational system initialized at 1200 UTC 6 August. There is no obvious
419 difference at 0000 UTC 8 August, whereas NICAM showed apparent differences
420 (Fig. 5). However, by 10 August, WNPSH retreated more eastward with the
421 worst members than with the best members. In addition, Krosa's northward
422 movement was faster at all centers, and Lekima's northward movement was
423 slower at all centers with the worst members except for JMA. Thus, with the
424 worst members, Krosa and Lekima would rotate around each other in an
425 anticlockwise direction. Overall, these results suggest that, as found in the
426 NICAM simulations, at least the stronger interaction between Krosa and Lekima
427 would occur with the worst members than with the best members and that it is
428 associated with the eastward retreat of WNPSH.

Fig. 15

5. Summary and Conclusion

In this study, the main cause of the uncertainty in forecasting Krosa's track, as seen in the operational ensemble forecast data, was examined by a 101-member ensemble forecast by NICAM, which was initialized using the LETKF-based data assimilation product NEXRA. The large uncertainty in the model initialized at 1200 UTC 6 August and the decrease in uncertainty as the model initialization time went by, as predicted by the operational systems, were successfully reproduced by NICAM. The ensemble-based sensitivity analysis of Krosa's track forecast error suggested that the track error was sensitive to the intensity of WNPSH over Japan and the distance between Krosa and Lekima. The best and worst members (20 for each) in terms of Krosa's forecast track error were compared. The westward extension of WNPSH was stronger with the best members, and the northward movement of Krosa was faster with the worst members. The distance between Krosa and Lekima decreased by 250 km in 36 hours after the model initialization time with the worst members, whereas the distance was almost constant in 24 hours after the model initialization time with the best members. These results suggest that a strong interaction between Krosa and Lekima occurred with the worst members, leading to a fast northward movement and a large track forecast error.

The difference in the composite fields between the best and worst members indicates that Krosa had a larger vortex size with the worst members than with the best members at the initial conditions. However, little differences were found around Lekima. The Krosa's larger vortex size with the worst members at the model initial time led to larger vortex size with the worst members of the NICAM forecasts. This larger storm size with the worst member should result in retreat

of the WNPSH through the mechanism proposed by Sun et al. (2015) and lead to faster northward movement of Krosa. These results suggest that the analysis error of the meteorological field including the TC position around Krosa in NEXRA, which was used in the NICAM forecasts, determines whether a strong interaction between Krosa and Lekima and the retreat of WNPSH would occur or not. The analysis of the operational models suggests that at least strong interaction between two TCs occurred with the worst members also worked in these models whereas the timing is later than NICAM.

Considering that BSISO sometimes causes multiple TC formations, such as in the present case, examining whether the track forecast busts associated with BSISO occur or not is the next step to further improve TC forecasting. Lekima and Krosa were formed under a convective envelope associated with BSISO. There is a possibility that it was difficult to obtain enough observational data to constrain the model, especially at the initial phase of Krosa. Recent studies have shown that assimilating all-sky radiance data improves TC forecasting (Honda et al. 2018; Minamide and Zhang 2018). Assimilating satellite-based synthetic aperture radar (SAR) is also promising because SAR can retrieve high surface wind speed (> 20 m s^{-1}) even in cloudy/rain areas. Thus, implementing such advanced methods to NEXRA as well as increasing special resolution of NEXRA for better use of these data and quantifying the improvement rate of TC forecasting under many cases (e.g., Nakano et al. 2017) would be useful in future works.

Data Availability Statement

The NEXRA analysis data are available upon request to the NEXRA development team (Z-NEXRA_ADMIN@ml.jaxa.jp). All the data from ensemble experiments by NICAM will be provided from M.N. upon request.

Supplement

None

Acknowledgments

The authors thank the editor and two anonymous reviewers for their helpful comments. This work was supported by MEXT (JPMXP1020351142) as “Program for Promoting Researches on the Supercomputer Fugaku” (Large Ensemble Atmospheric and Environmental Prediction for Disaster Prevention and Mitigation) and KAKENHI (JP20H05728 and JP20H05730). All the simulation was performed on the 3rd generation of the Earth Simulator (NEC SX-ACE) of JAMSTEC and the simulation data was post-processed on the data analyzer of JAMSTEC. The TIGGE data was obtained from MARS system of ECMWF. The ensemble analysis data obtained from NEXRA are produced on the second generation JAXA’s supercomputer system (JSS2). The TC tracking tool was provided by Dr. M. Sawada of JMA.

References

Ancell, B., and G. J. Hakim, 2007: Comparing Adjoint- and Ensemble-Sensitivity Analysis with Applications to Observation Targeting. *Mon. Weather Rev.*, **135**, 4117–4134, https://doi.org/10.1175/2007MWR1904.1.

Bougeault, P., and Coauthors, 2010: The THORPEX Interactive Grand Global Ensemble. *Bull. Am. Meteorol. Soc.*, **91**, 1059–1072, https://doi.org/10.1175/2010BAMS2853.1.

Brand, S., 1970: Interaction of Binary Tropical Cyclones of the Western North Pacific Ocean. *J. Appl. Meteorol. Climatol.*, **9**, 433–441, https://doi.org/10.1175/1520-0450(1970)009<0433:IOBTCO>2.0.CO;2.

Camp, J., and Coauthors, 2019: The western Pacific subtropical high and tropical cyclone landfall: Seasonal forecasts using the Met Office GloSea5 system. *Quart. J. Roy. Meteor. Soc.*, **145**, 105–116, https://doi.org/10.1002/qj.3407.

Choi, K.-S., C.-C. Wu, and E.-J. Cha, 2010: Change of tropical cyclone activity by Pacific-Japan teleconnection pattern in the western North Pacific. *J. Geophys. Res.*, **115**, https://doi.org/10.1029/2010jd013866.

Choi, Y., D.-H. Cha, M.-I. Lee, J. Kim, C.-S. Jin, S.-H. Park, and M.-S. Joh, 2017: Satellite radiance data assimilation for binary tropical cyclone cases over the western N orth P acific. *J. Adv. Model. Earth Syst.*, **9**, 832–853, https://doi.org/10.1002/2016ms000826.

Corbosiero, K. L., and J. Molinari, 2002: The effects of vertical wind shear on the distribution of convection in tropical cyclones. *Mon. Weather Rev.*, **130**, 2110–2123.

Fujiwhara, S., 1921: The natural tendency towards symmetry of motion and its application as a principle in meteorology. *Quart. J. Roy. Meteor. Soc.*, **47**, 287–292, https://doi.org/10.1002/qj.49704720010.

——, 1923: On the growth and decay of vortical systems. *Quart. J. Roy. Meteor. Soc.*, **49**, 75–104, https://doi.org/10.1002/qj.49704920602.

Honda, T., and Coauthors, 2018: Assimilating All-Sky Himawari-8 Satellite Infrared Radiances: A Case of Typhoon Soudelor (2015). *Mon. Weather Rev.*, **146**, 213–229, https://doi.org/10.1175/MWR-D-16-0357.1.

Hunt, B. R., E. J. Kostelich, and I. Szunyogh, 2007: Efficient data assimilation for spatiotemporal chaos: A local ensemble transform Kalman filter. *Physica D*, **230**, 112–126, https://doi.org/10.1016/j.physd.2006.11.008.

Ito, K., and H. Ichikawa, 2021: Warm Ocean Accelerating Tropical Cyclone Hagibis (2019) through Interaction with a Mid-Latitude Westerly Jet. *SOLA*, **17A**, 1–6.

Japan Meteorological Agency, 2020: *Annual Report on the Activities of the RSMC Tokyo - Typhoon Center 2019*. 115 pp.

https://www.jma.go.jp/jma/jma-eng/jma-center/rsmc-hp-pub-eg/AnnualReport/2019/Text/Text2019.pdf.

Kawamura, R., and T. Ogasawara, 2006: On the Role of Typhoons in Generating PJ Teleconnection Patterns over the Western North Pacific in Late Summer. *SOLA*, **2**, 37–40, https://doi.org/10.2151/sola.2006-010.

Kikuchi, K., 2021: The Boreal Summer Intraseasonal Oscillation (BSISO): A Review. *Journal of Meteorological Society of Japan*, **99**, 933–972, https://doi.org/10.2151/jmsj.2021-045.

Kodama, C., and Coauthors, 2021: The Nonhydrostatic ICosahedral Atmospheric Model for CMIP6 HighResMIP simulations (NICAM16-S): experimental design, model description, and impacts of model updates. *Geoscientific Model Development*, **14**, 795–820, https://doi.org/10.5194/gmd-14-795-2021.

Kotsuki, S., K. Terasaki, K. Kanemaru, M. Satoh, T. Kubota, and T. Miyoshi, 2019: Predictability of record-breaking rainfall in Japan in July 2018: Ensemble forecast experiments with the near-real-time global atmospheric data assimilation system NEXRA. *Scientific Online Letters on the Atmosphere*, **15**, 1–7, https://doi.org/10.2151/SOLA.15A-001.

Kotsuki, S., T. Miyoshi, and K. Terasaki, 2017: Assimilating the global satellite mapping of precipitation data with the Nonhydrostatic Icosahedral Atmospheric Model (NICAM). *J. Geophys. Res. Atmos.*, **122**, 631– 650, https://doi.org/10.1002/2016JD025355.

Lu, R., and B. Dong, 2001: Westward Extension of North Pacific Subtropical High in Summer. *Journal of the Meteorological Society of Japan*, **79**, 1229–1241, https://doi.org/10.2151/jmsj.79.1229.

Magnusson, L., J.-R. Bidlot, S. T. K. Lang, A. Thorpe, N. Wedi, and M. Yamaguchi, 2014: Evaluation of Medium-Range Forecasts for Hurricane Sandy. *Mon. Weather Rev.*, **142**, 1962–1981, https://doi.org/10.1175/MWR-D-13-00228.1.

Minamide, M., and F. Zhang, 2018: Assimilation of All-Sky Infrared Radiances from Himawari-8 and Impacts of Moisture and Hydrometer Initialization on Convection-Permitting Tropical Cyclone Prediction. *Mon. Weather Rev.*, **146**, 3241–3258, https://doi.org/10.1175/MWR-D-17-0367.1.

Nakano, M., and Coauthors, 2017: Global 7 km mesh nonhydrostatic Model Intercomparison Project for improving TYphoon forecast (TYMIP-G7): experimental design and preliminary results. *Geoscientific Model Development*, **10**, 1363–1381, https://doi.org/10.5194/gmd-10-1363-2017.

Nakano, M., F. Vitart, and K. Kikuchi, 2021: Impact of the boreal summer intraseasonal oscillation on typhoon tracks in the western north pacific

and the prediction skill of the ECMWF model. *Geophys. Res. Lett.*, **48**, https://doi.org/10.1029/2020gl091505.

Nakashita, S., and T. Enomoto, 2021: Factors for an Abrupt Increase in Track Forecast Error of Typhoon Hagibis (2019). *SOLA*, **17A**, 33-37, https://doi.org/10.2151/sola.17A-006.

Nakazawa, T., and K. Rajendran, 2007: Relationship between Tropospheric Circulation over the Western North Pacific and Tropical Cyclone Approach/Landfall on Japan. *J. Meteorol. Soc. Japan*, **85**, 101–114, https://doi.org/10.2151/jmsj.85.101.

Nitta, T., 1987: Convective activities in the tropical western Pacific and their impact on the Northern Hemisphere summer circulation. *J. Meteorol. Soc. Japan*, **65**, 373–390.

Nolan, D. S., M. T. Montgomery, and L. D. Grasso, 2001: The Wavenumber-One Instability and Trochoidal Motion of Hurricane-like Vortices. *J. Atmos. Sci.*, **58**, 3243–3270.

Peng, M. S., and C. A. Reynolds 2005: Double trouble for typhoon forecasters. *Geophys. Res. Lett.*, **32**, https://doi.org/10.1029/2004gl021680.

Roh, W., and M. Satoh, 2014: Evaluation of Precipitating Hydrometeor Parameterizations in a Single-Moment Bulk Microphysics Scheme for Deep Convective Systems over the Tropical Central Pacific. *J. Atmos. Sci.*, **71**, 2654–2673, https://doi.org/10.1175/JAS-D-13-0252.1.

Satoh, M., and Coauthors, 2014: The Non-hydrostatic Icosahedral Atmospheric Model: description and development. *Progress in Earth and Planetary Science*, **1**, 1–32, https://doi.org/10.1186/s40645-014-0018-1.

Sun, Y., Z. Zhong, L. Yi, T. Li, M. Chen, H. Wan, Y. Wang, and K. Zhong, 2015: Dependence of the relationship between the tropical cyclone track and western Pacific subtropical high intensity on initial storm size: A numerical investigation. *J. Geophys. Res.*, **120**, 11,451-11,467.

Swinbank, R., and Coauthors, 2016: The TIGGE Project and Its Achievements. *Bull. Am. Meteorol. Soc.*, **97**, 49–67, https://doi.org/10.1175/BAMS-D-13-00191.1.

Terasaki, K., and T. Miyoshi, 2017: Assimilating AMSU-A Radiances with the NICAM-LETKF. *J. Meteor. Soc. Jpn.*, **95**, 433–446.

Torn, R. D., and G. J. Hakim, 2008: Ensemble-Based Sensitivity Analysis. *Mon. Weather Rev.*, **136**, 663–677, https://doi.org/10.1175/2007MWR2132.1.

Ueno, M., 2007: Observational Analysis and Numerical Evaluation of the Effects of Vertical Wind Shear on the Rainfall Asymmetry in the Typhoon Inner-Core Region. *Journal of the meteorological society of Japan*, **85**, 115–136.

Velden, C. S., and L. M. Leslie, 1991: The Basic Relationship between Tropical Cyclone Intensity and the Depth of the Environmental Steering Layer in the Australian Region. *Weather Forecast.*, **6**, 244–253.

Wang, B., and H. Rui, 1990: Synoptic climatology of transient tropical intraseasonal convection anomalies: 1975-1985. *Meteorol. Atmos. Phys.*, **44**, 43–61, https://doi.org/10.1007/BF01026810.

Wang, B., and X. Xie, 1997: A model for the boreal summer intraseasonal oscillation. *J. Atmos. Sci.*, **54**, 72–86, https://doi.org/10.1175/1520-0469(1997)054<0072:AMFTBS>2.0.CO;2.

628 List of Figures

629

630 Fig. 1. Track forecast for Krosa (2019) by the ECMWF (a–d), JMA (e–h), and
631 NCEP (i–l) models, initialized at 1200 UTC 6 August (a, e, i); 1200 UTC 7
632 August (b, f, j); 1200 UTC 8 August (c, g, k); and 1200 UTC 9 August (d, h, l),
633 respectively. The color indicates the valid date (day of August starting from
634 1200 UTC). The best track is also shown by thick color line surrounded by
635 black.

636

637 Fig. 2. Track forecast for Krosa by NICAM initialized at 1200 UTC 6 August (a);
638 1200 UTC 7 August (b); 1200 UTC 8 August (c); and 1200 UTC 9 August (d),
639 respectively. The color indicates the valid date (day of August starting from
640 1200 UTC). The best track is also shown by thick color line surrounded by
641 black.

642

643 Fig. 3. Ensemble-based lagged correlation (shade) between the 500-hPa
644 geopotential height for 1200 UTC 6 August (a); 0000 UTC 7 August (b); 1200
645 UTC 7 August (c); and 0000 UTC 8 August (d) and Krosa's track forecast error
646 at 1200 UTC 11 August. The contours show the 500-hPa geopotential height
647 (m) simulated in the experiment initialized with the ensemble-mean of 100-
648 member analyses.

649

650 Fig. 4. Clustered track forecast for Krosa (a–b) and Lekima (c–d), initialized at
651 1200 UTC 6 August by the track forecast error for Krosa at 1200 UTC 11
652 August. Best 20 members (a and c), worst 20 members (b and d). The color

indicates the valid date (day of August starting from 1200 UTC). The best track is also shown by thick color line surrounded by black.

Fig. 5. Spaghetti diagram of the 500-hPa geopotential height valid for 0000 UTC of (a) 7 August; (b) 8 August; and (c) 9 August, respectively. The orange (aqua) contours are forecasted by the worst (best) 20 members, and the thick lines are ensemble means of the best and worst members. The contours for 5760 (broken line) and 5860 (solid line) m are shown.

Fig. 6. Six-hourly ensemble means of the best (blue) and worst members (red) (a) Track forecast, (b) track forecast error (km), (c) distance between Lekima and Krosa (km), and (d) minimum sea level pressure (hPa). The plus (+) and cross (x) symbols in (a, b, and d) are for Lekima and Krosa, respectively. The minimum sea level pressure in the best track data is also shown by black curves and symbols in d.

Fig. 7. Distributions of the TC center position (cross symbols) and SLP (contours; hPa) at FT = 1 h (a, c) and FT = 12 h (b, d) for Krosa (a–b) and Lekima (c–d) simulated for the best (blue) and worst (red) members. The black cross symbols indicate Krosa's (a–b) and Lekima's (c–d) position analyzed in the best track at 1200 UTC 6 August (a and c) and 0000 UTC 7 August. The existence frequencies of TC center for each latitude and longitude bin (size = 0.5°) are also shown in the left and bottom sub-panel, respectively.

Fig. 8. Ensemble means of (a-b) the geopotential height at 925 hPa (Z925; m),

(e-f) 10-m winds (vector; m s^{-1}) and 10-m wind speed (shade; m s^{-1}), analyzed in NEXRA for the ensemble mean of the best (a, e) and worst (b, f) 20 members at 1200 UTC 6 August and their differences (c, g) around Krosa. The x and y axes represent the eastward and northward distance (degree) from Krosa's center, respectively. The ensemble-based lagged correlation between (d) Z925 and (h)10-m wind speed and Krosa's track forecast error at 1200 UTC 11 August are also shown. The thick black contours in a and b are for 680 m of Z925.

Fig. 9. Same as Fig. 8 but for around Lekima.

Fig. 10. TC-center relative ensemble-based lagged correlation between (a, c) SLP and (b, d)10-m wind speed and Krosa's track forecast error at 1200 UTC 11 August for (a, b) 1800 UTC 6 August (FT = 6 h) and (c, d) 1200 UTC 7 August (FT = 24 h). The x and y axes represent the eastward and northward distance (degree) from Krosa's center, respectively.

Fig. 11. Ensemble mean of the horizontal winds (vector; m s^{-1}), divergence (shade; s^{-1}) and geopotential height (contour; m) at 200 hPa for the best (a–c) and worst (d–f) members and their difference (g–i) at 0000 UTC 7 August (a, d, g); 0000 UTC 8 August (b, e, h); and 0000 UTC 9 August (c, f, g), respectively. The blue and red crosses are ensemble mean of TC centers for the best and worst members, respectively. Thick broken lines in a–f show the radius of 6 and 9.5 degree from the Krosa's center for reference.

703 Fig. 12. Same as Fig. 11 but for 925 hPa.

704

705 Fig. 13. The vertical wind shear of horizontal winds between 11988 m and 1500
706 m at 0000 UTC 7 August (red); 8 August (green); and 9 August (blue),
707 respectively. The x and y axes are the zonal and meridional component (m s^{-1}).

708

709 Fig. 14. Ensemble-based lagged correlation between the divergence averaged
710 (a) within 6 degrees and (b) between 6 and 9.5 degrees from the Krosa's center
711 and Krosa's track forecast error at 1200 UTC 11 August, respectively.

712

713 Fig. 15. Spaghetti diagram of the 500-hPa geopotential height valid for (a, d, g)
714 0000 UTC 8 August; (b, e, h) 0000 UTC 9 August; and (c, f, i) 0000 UTC 10
715 August by the ECMWF (a–c), JMA (d–f), and NCEP (g–i) models, initialized at
716 1200 UTC 6 August. The thin orange (aqua) contours were forecasted by the
717 worst (best) 20% (10 for ECMWF, 5 for JMA, 4 for NCEP) of the members in
718 terms of the Krosa track forecast error at 1200 UTC 11 August. The thick lines
719 are ensemble means of the best and worst members, respectively. The black
720 contours show the analysis by each model. The contours for 5760 (broken line)
721 and 5860 (solid line) m are shown.

722

723

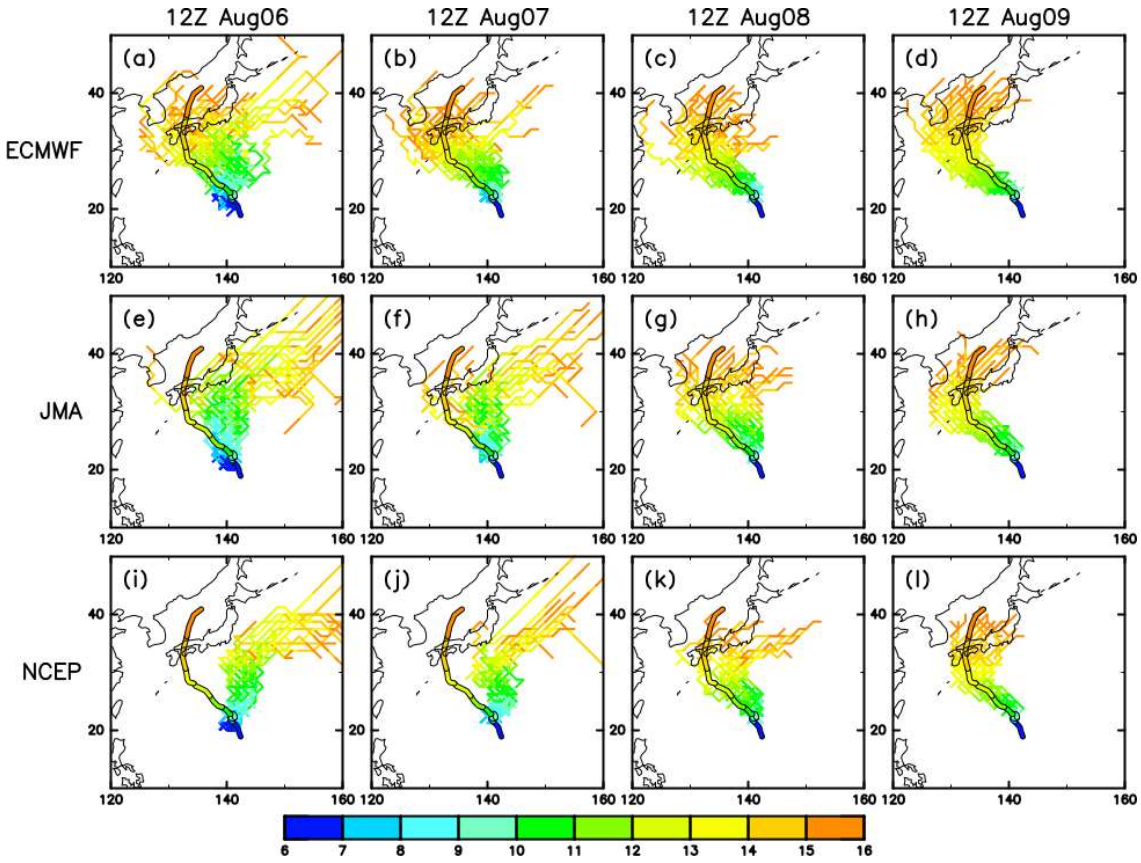

Fig. 1 Track forecast for Krosa (2019) by the ECMWF (a–d), JMA (e–h), and NCEP (i–l) models, initialized at 1200 UTC 6 August (a, e, i); 1200 UTC 7 August (b, f, j); 1200 UTC 8 August (c, g, k); and 1200 UTC 9 August (d, h, l), respectively. The color indicates the valid date (day of August starting from 1200 UTC). The best track is also shown by thick color line surrounded by black.

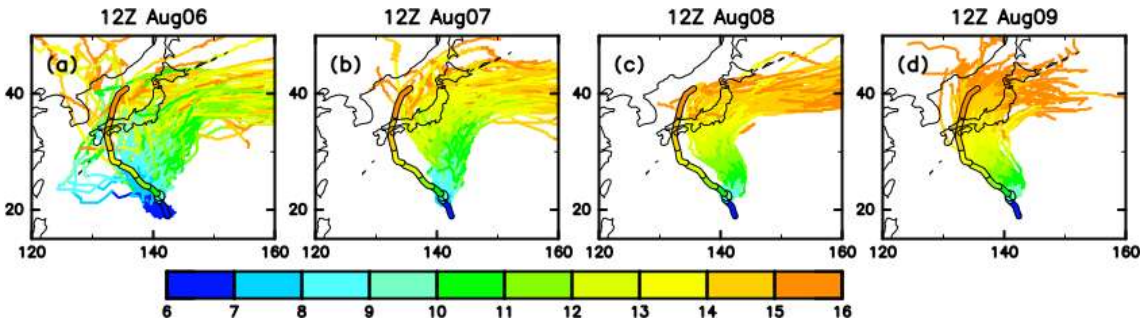

Fig. 2 Track forecast for Krosa by NICAM initialized at 1200 UTC 6 August (a); 1200 UTC 7 August (b); 1200 UTC 8 August (c); and 1200 UTC 9 August (d), respectively. The color indicates the valid date (day of August starting from 1200 UTC). The best track is also shown by thick color line surrounded by black.

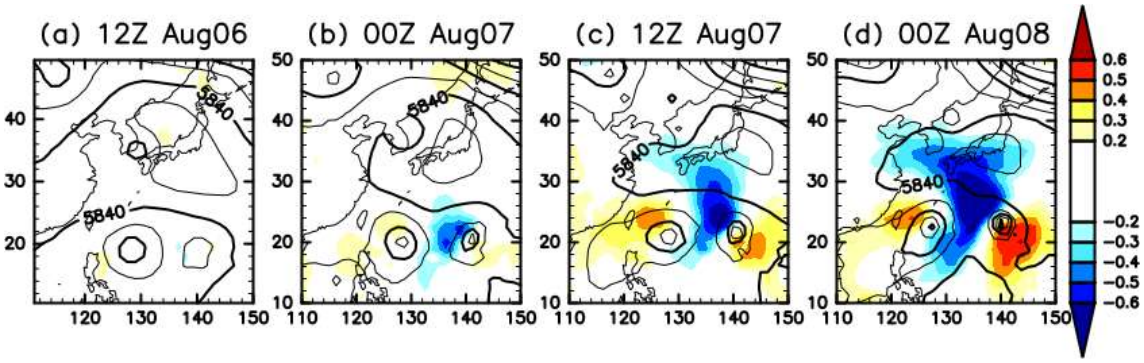

745
746

747 Fig. 3 Ensemble-based lagged correlation (shade) between the 500-hPa

748 geopotential height for 1200 UTC 6 August (a); 0000 UTC 7 August (b); 1200

749 UTC 7 August (c); and 0000 UTC 8 August (d) and Krosa's track forecast

750 error at 1200 UTC 11 August. The contours show the 500-hPa geopotential

751 height (m) simulated in the experiment initialized with the ensemble-mean of

752 100-member analyses.

753
754

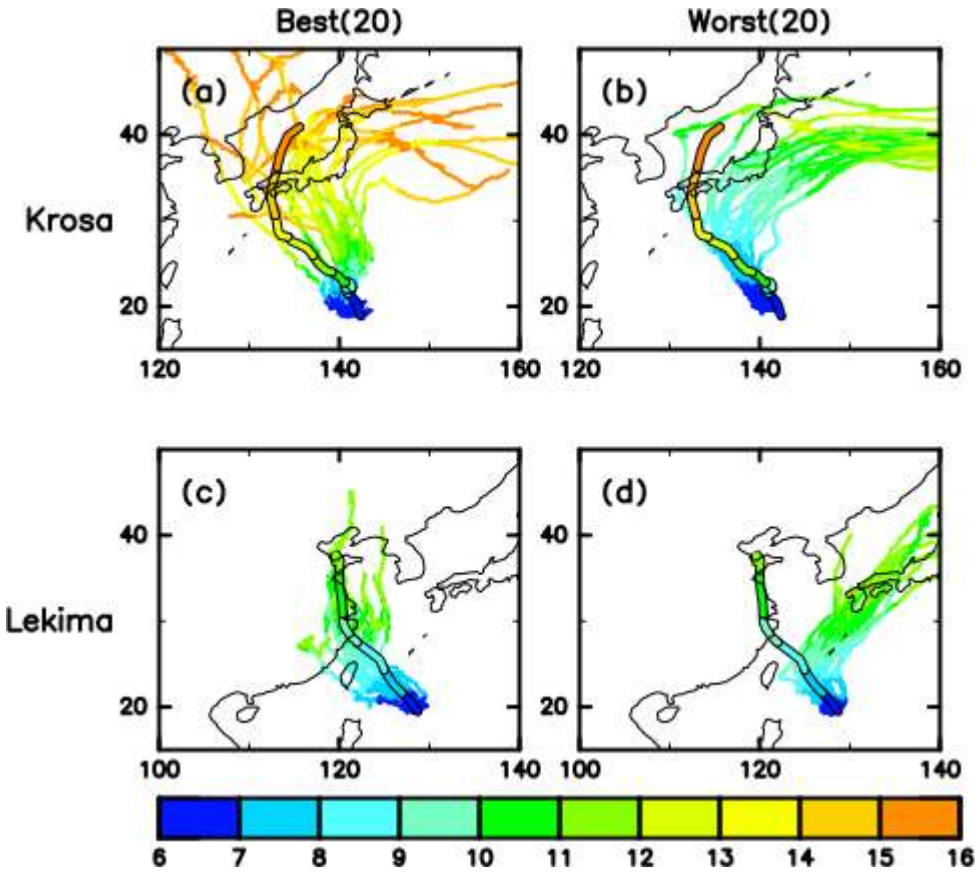

Fig. 4 Clustered track forecast for Krosa (a–b) and Lekima (c–d), initialized at 1200 UTC 6 August by the track forecast error for Krosa at 1200 UTC 11 August. Best 20 members (a and c), worst 20 members (b and d). The color indicates the valid date (day of August starting from 1200 UTC). The best track is also shown by thick color line surrounded by black.

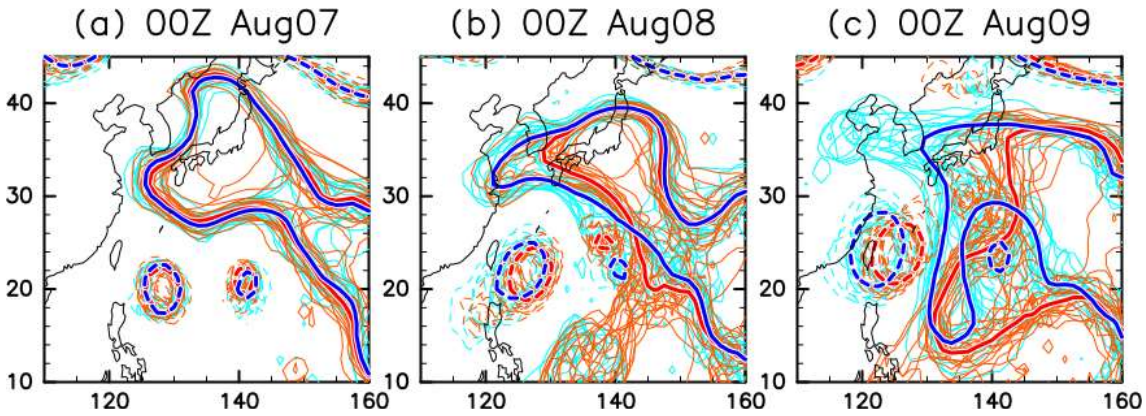

Fig. 5 Spaghetti diagram of the 500-hPa geopotential height valid for 0000 UTC of (a) 7 August; (b) 8 August; and (c) 9 August, respectively. The orange (aqua) contours are forecasted by the worst (best) 20 members, and the thick lines are ensemble means of the best and worst members. The contours for 5760 (broken line) and 5860 (solid line) m are shown.

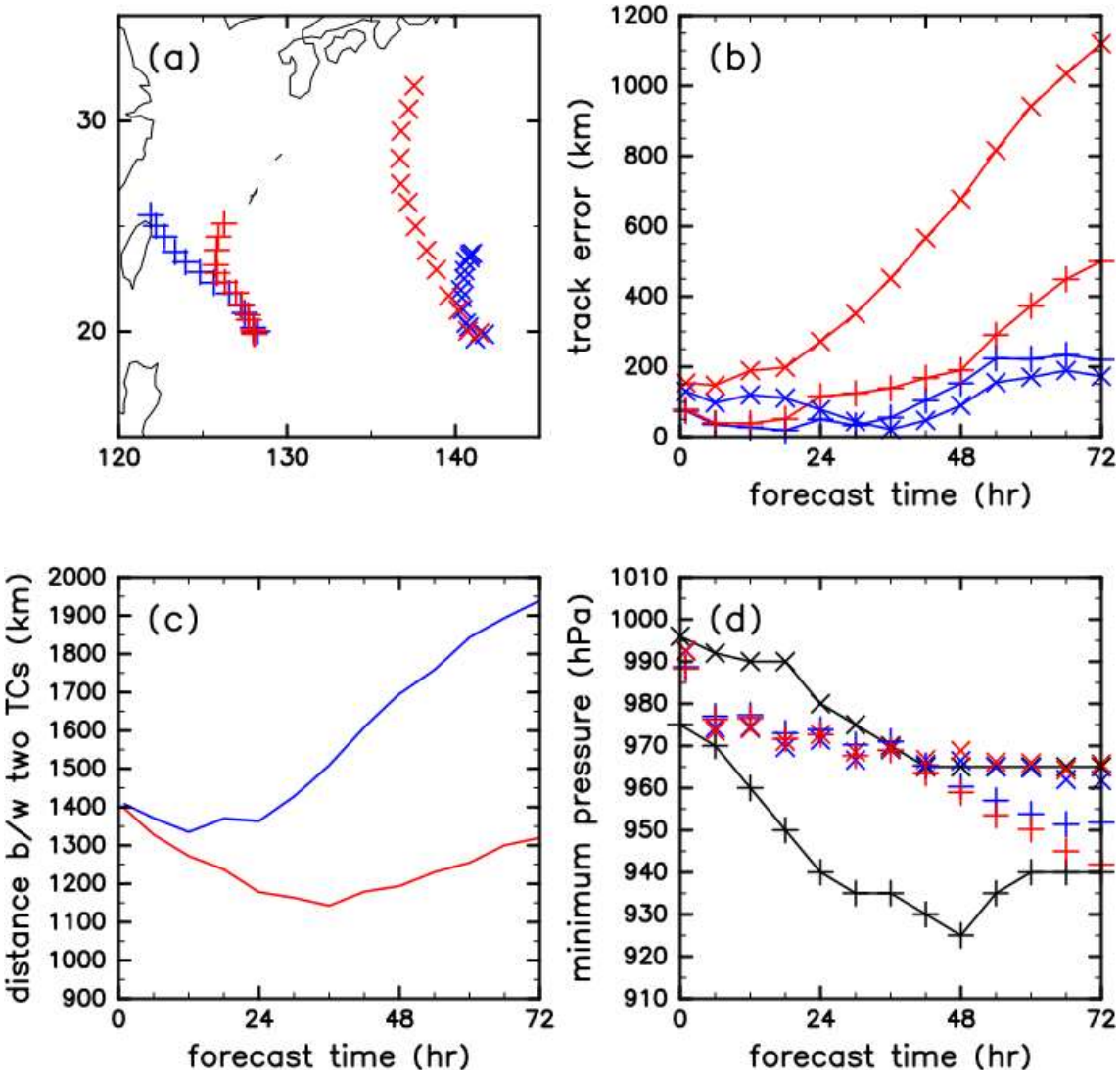

774
775

776 Fig. 6 Six-hourly ensemble means of the best (blue) and worst members (red)

777 (a) Track forecast, (b) track forecast error (km), (c) distance between Lekima

778 and Krosa (km), and (d) minimum sea level pressure (hPa). The plus (+) and

779 cross (x) symbols in (a, b, and d) are for Lekima and Krosa, respectively. The

780 minimum sea level pressure in the best track data is also shown by black

781 curves and symbols in d.

782
783
784

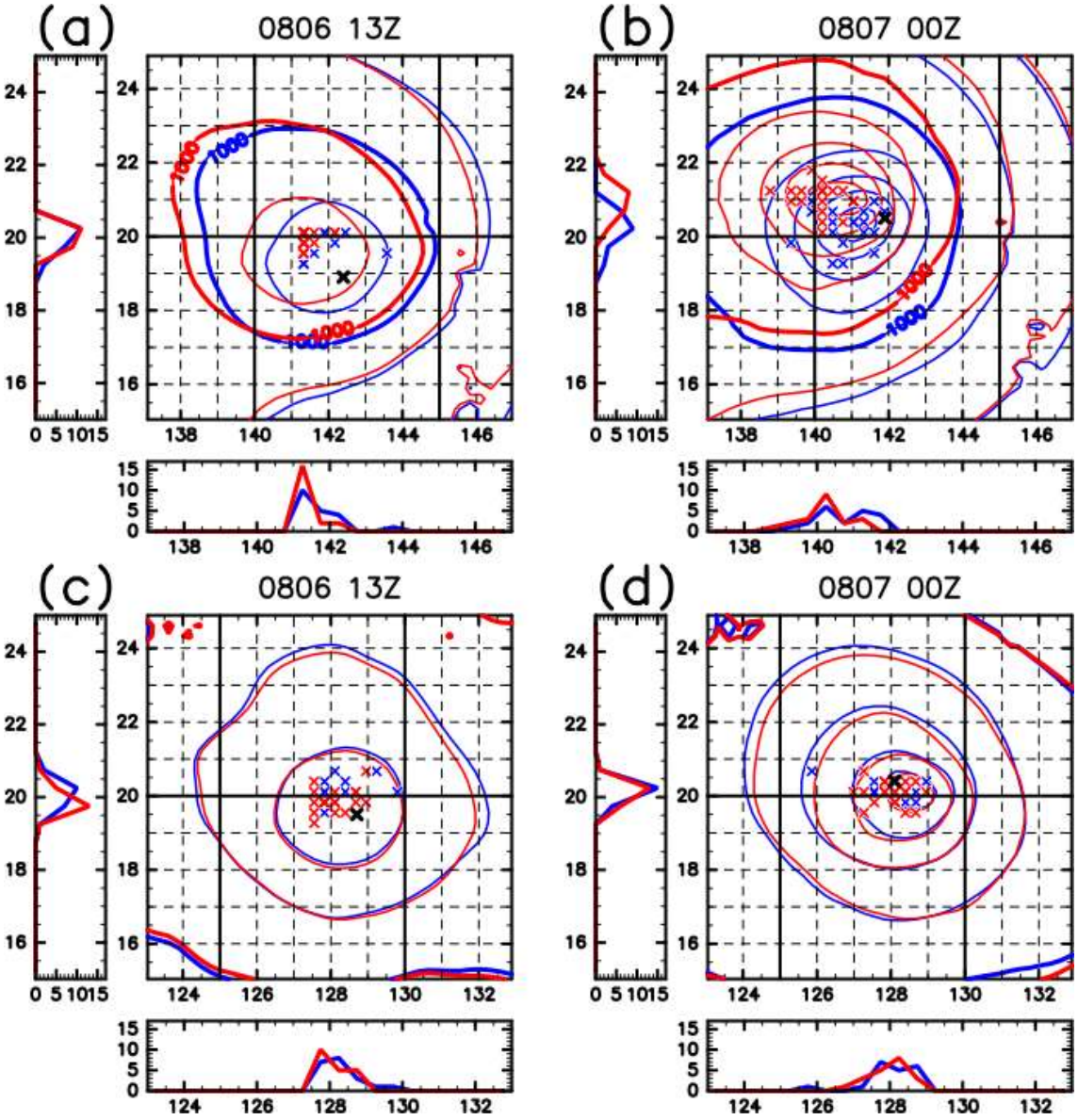

Fig. 7 Distributions of the TC center position (cross symbols) and SLP (contours; hPa) at FT = 1 h (a, c) and FT = 12 h (b, d) for Krosa (a–b) and Lekima (c–d) simulated for the best (blue) and worst (red) members. The black cross symbols indicate Krosa's (a–b) and Lekima's (c–d) position analyzed in the best track at 1200 UTC 6 August (a and c) and 0000 UTC 7 August. The existence frequencies of TC center for each latitude and longitude bin (size = 0.5°) are also shown in the left and bottom sub-panel, respectively.

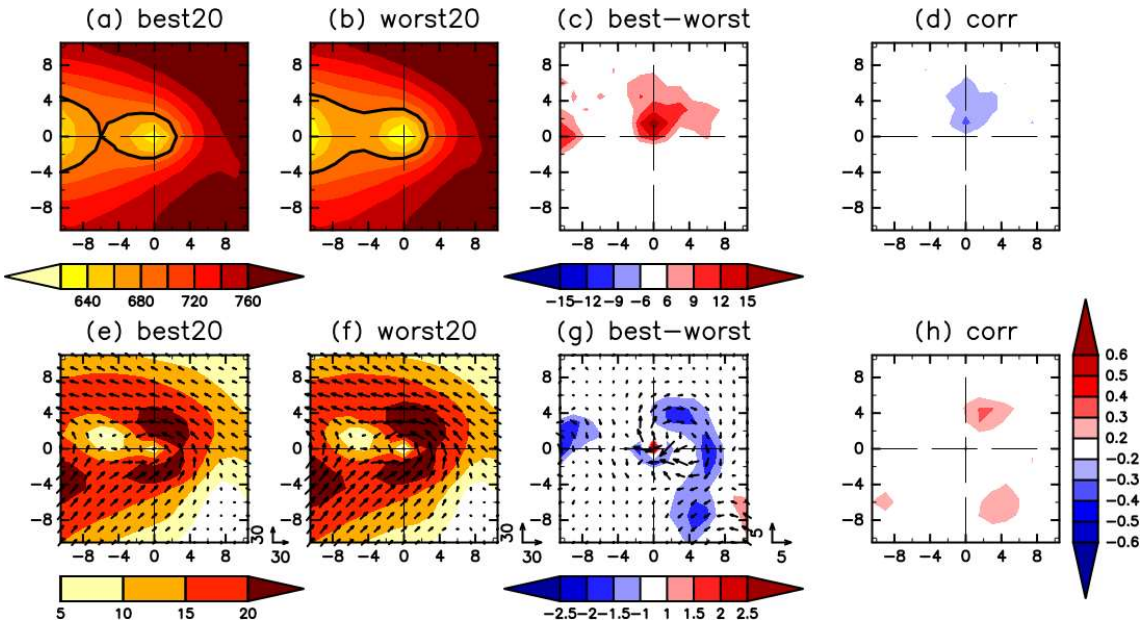

798
799
800 Fig. 8 Ensemble means of (a-b) the geopotential height at 925 hPa (Z925; m),
801 (e-f) 10-m winds (vector; m s^{-1}) and 10-m wind speed (shade; m s^{-1}),
802 analyzed in NEXRA for the ensemble mean of the best (a, e) and worst (b, f)
803 20 members at 1200 UTC 6 August and their differences (c, g) around Krosa.
804 The x and y axes represent the eastward and northward distance (degree)
805 from Krosa's center, respectively. The ensemble-based lagged correlation
806 between (d) Z925 and (h)10-m wind speed and Krosa's track forecast error at
807 1200 UTC 11 August are also shown. The thick black contours in a and b are
808 for 680 m of Z925.
809
810

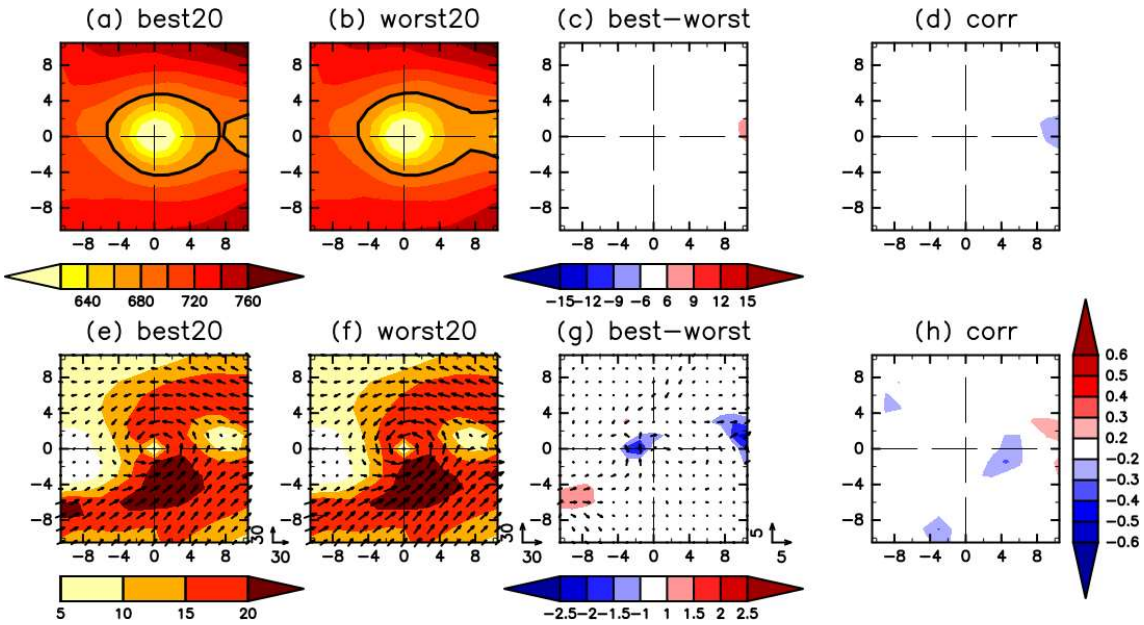

Fig. 9 Same as Fig. 8 but for around Lekima.

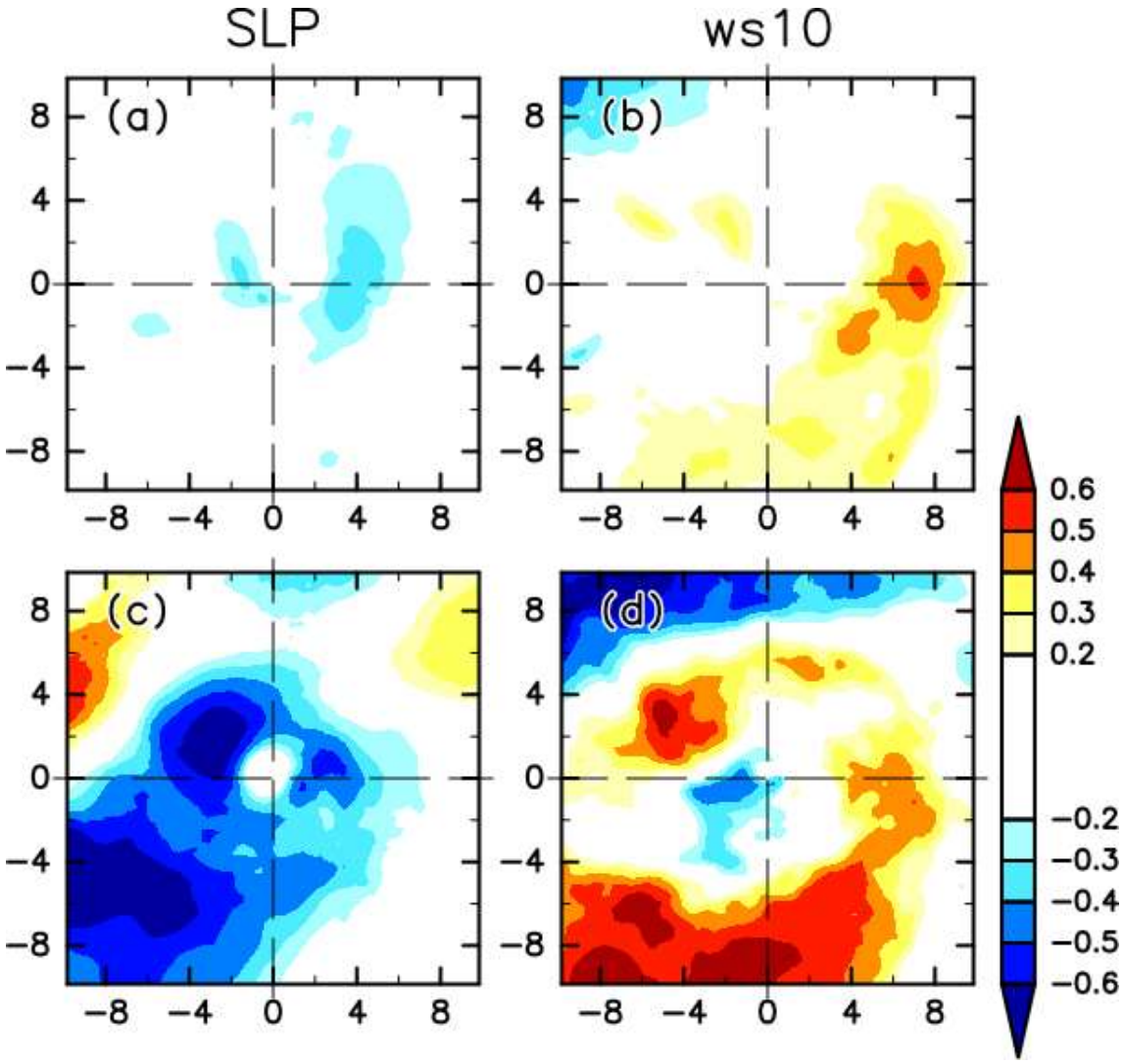

Fig. 10 TC-center relative ensemble-based lagged correlation between (a, c) SLP and (b, d)10-m wind speed and Krosa's track forecast error at 1200 UTC 11 August for (a, b) 1800 UTC 6 August (FT = 6 h) and (c, d) 1200 UTC 7 August (FT = 24 h). The x and y axes represent the eastward and northward distance (degree) from Krosa's center, respectively.

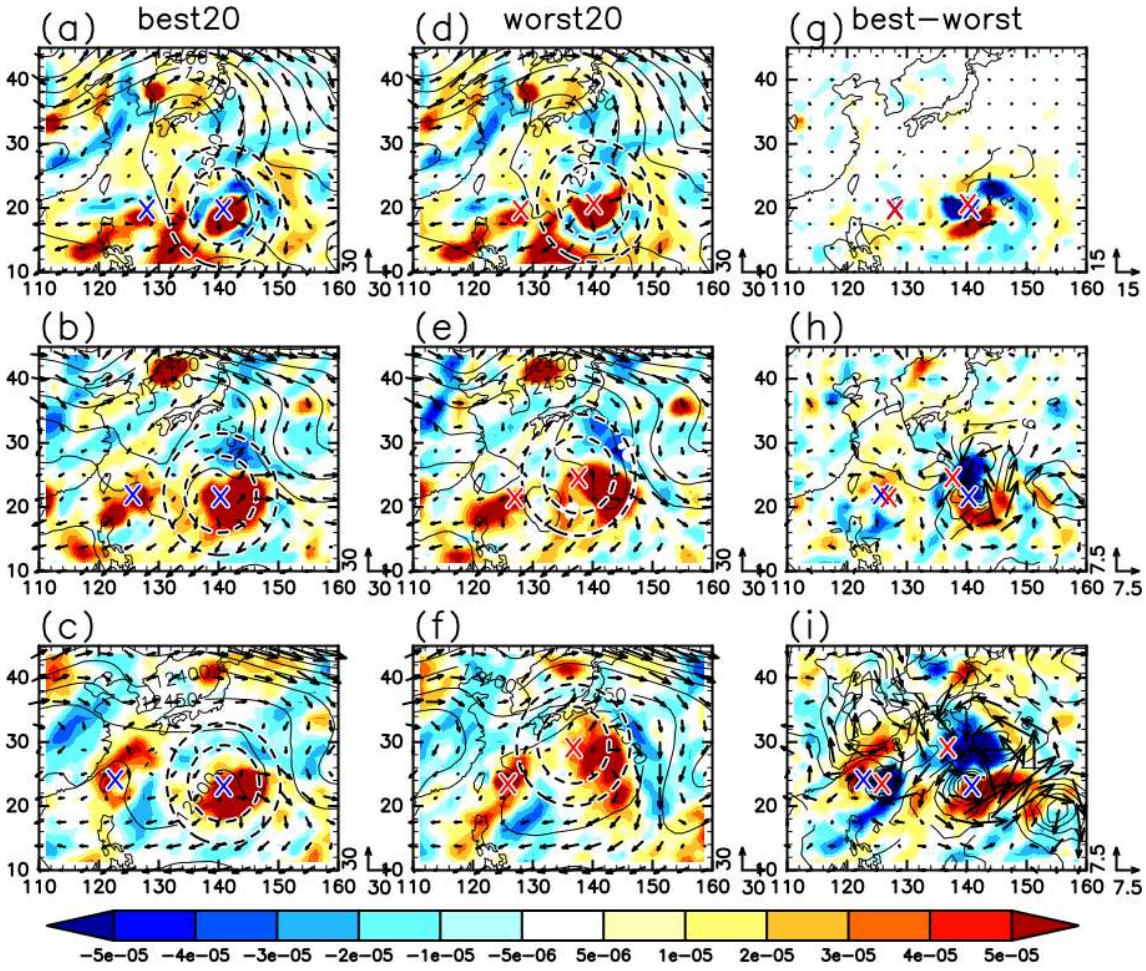

Fig. 11 Ensemble mean of the horizontal winds (vector; m s^{-1}), divergence (shade; s^{-1}) and geopotential height (contour; m) at 200 hPa for the best (a–c) and worst (d–f) members and their difference (g–i) at 0000 UTC 7 August (a, d, g); 0000 UTC 8 August (b, e, h); and 0000 UTC 9 August (c, f, g), respectively. The blue and red crosses are ensemble mean of TC centers for the best and worst members, respectively. Thick broken lines in a–f show the radius of 6 and 9.5 degree from the Krosa's center for reference.

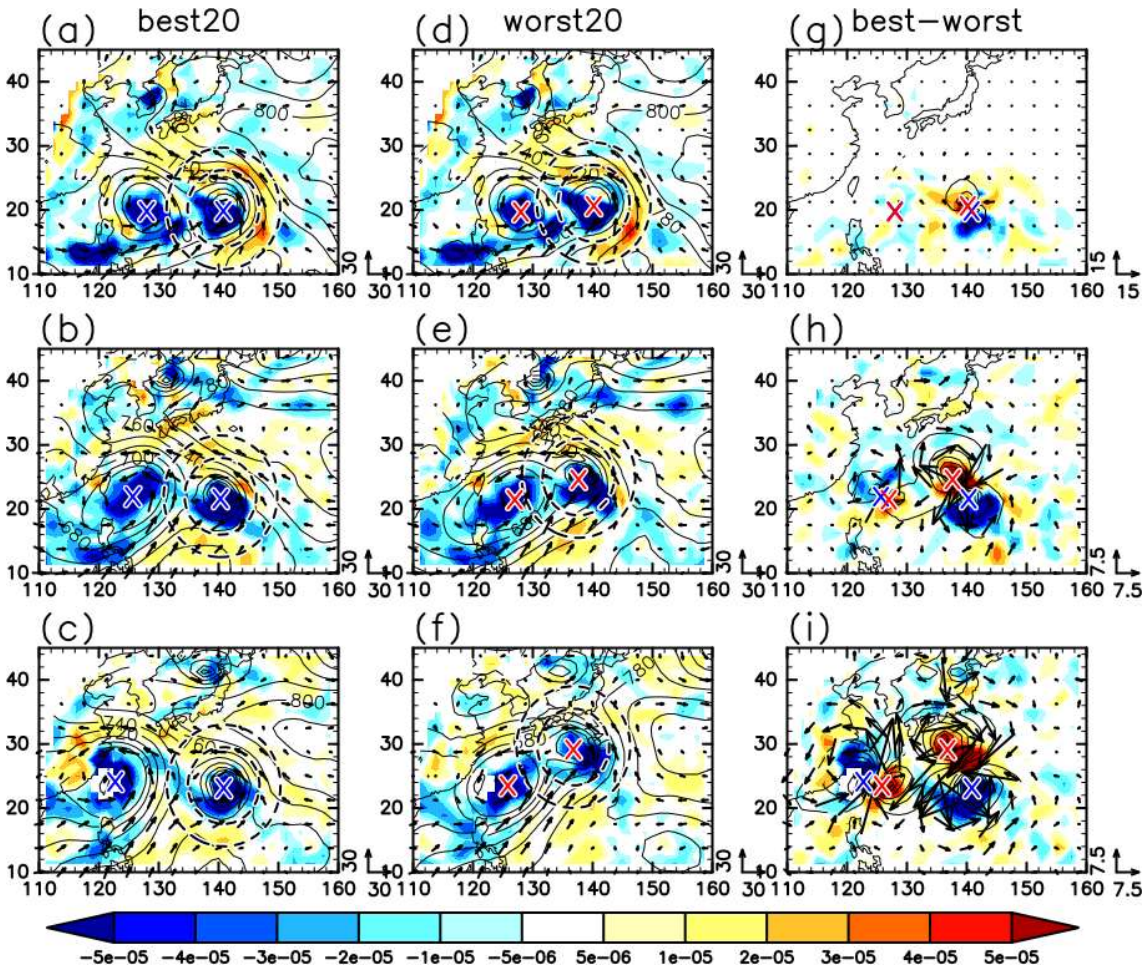

Fig. 12 Same as Fig. 11 but for 925 hPa.

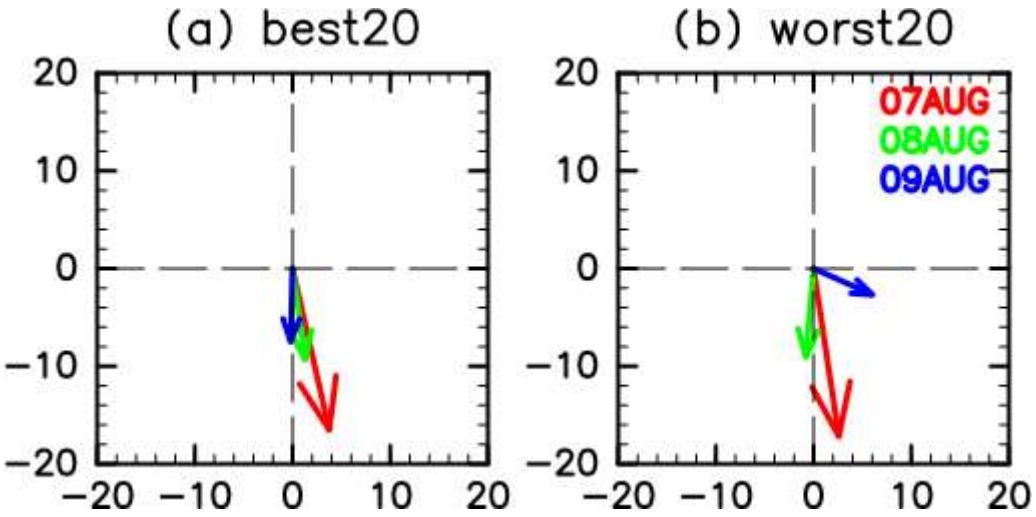

Fig. 13 The vertical wind shear of horizontal winds between 11988 m and 1500 m at 0000 UTC 7 August (red); 8 August (green); and 9 August (blue). The x and y axes are the zonal and meridional component (m s^{-1}), respectively.

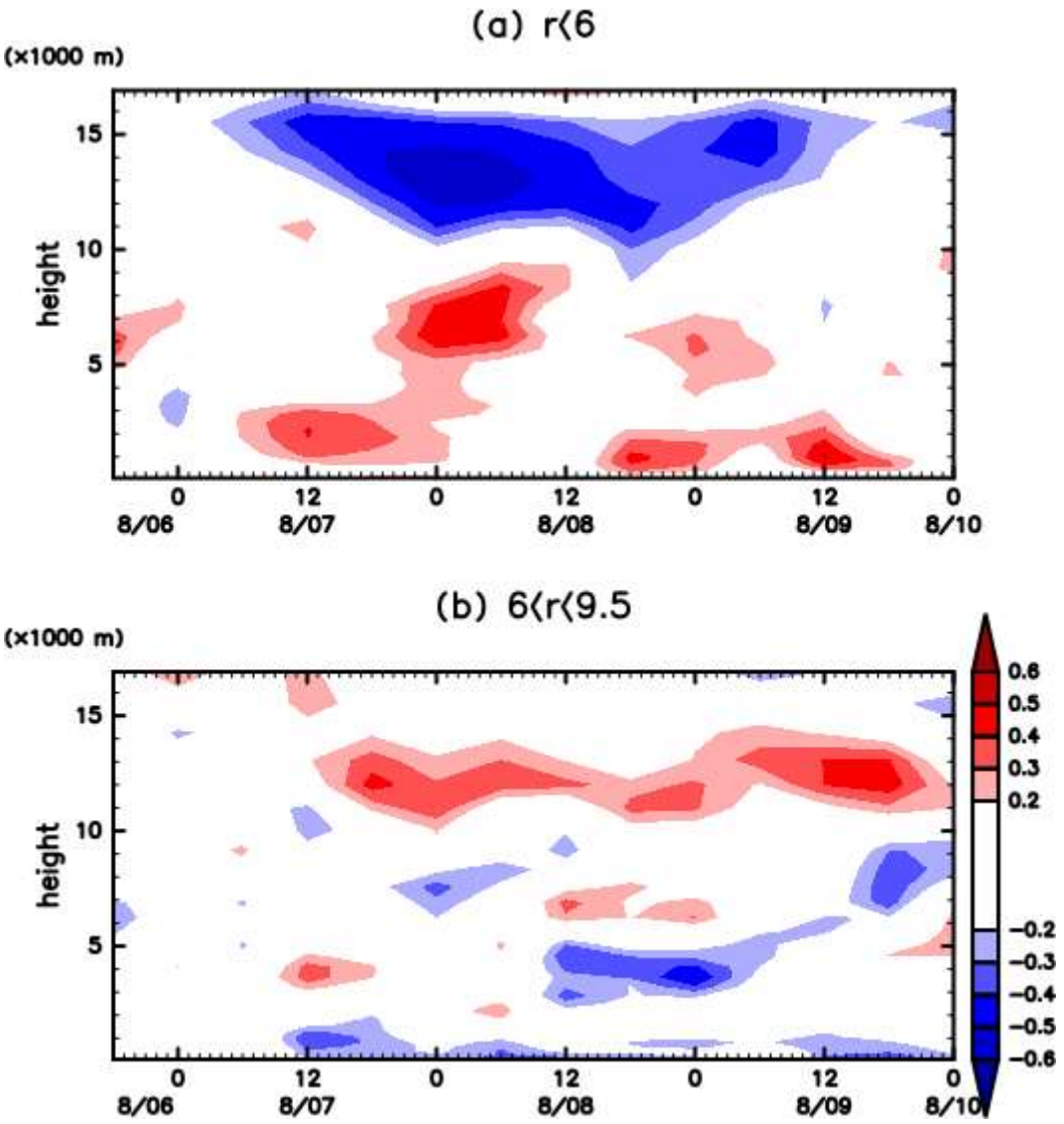

Fig. 14 Ensemble-based lagged correlation between the divergence averaged (a) within 6 degrees and (b) between 6 and 9.5 degrees from the Krosa's center and Krosa's track forecast error at 1200 UTC 11 August, respectively.

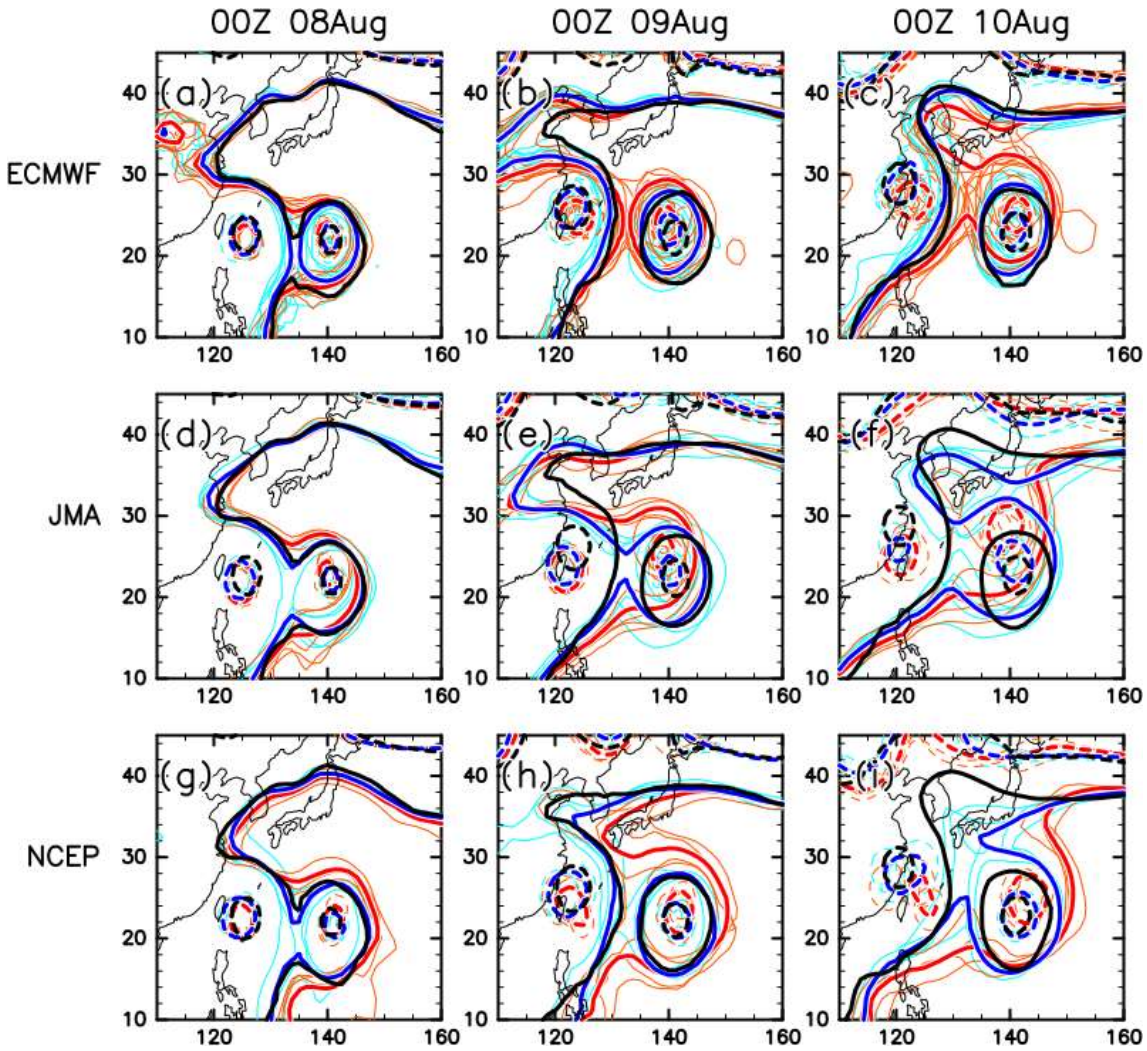

856

857

858 Fig. 15 Spaghetti diagram of the 500-hPa geopotential height valid for (a, d, g)
859 0000 UTC 8 August; (b, e, h) 0000 UTC 9 August; and (c, f, i) 0000 UTC 10
860 August by the ECMWF (a–c), JMA (d–f), and NCEP (g–i) models, initialized at
861 1200 UTC 6 August. The thin orange (aqua) contours were forecasted by the
862 worst (best) 20% (10 for ECMWF, 5 for JMA, 4 for NCEP) of the members in
863 terms of the Krosa track forecast error at 1200 UTC 11 August. The thick lines
864 are ensemble means of the best and worst members, respectively. The black
865 contours show the analysis by each model. The contours for 5760 (broken
866 line) and 5860 (solid line) m are shown.

867

868 List of Tables

869

870 Table 1. Specifications of the operational ensemble prediction data archived at
871 TIGGE.

872

873 Table 1 Specifications of the operational ensemble prediction data archived at
874 TIGGE as of August 2019.
875

	ECMWF	JMA	NCEP
Model resolution	Tco639 (Tco319 after 10 day)	TL479	TL574(TL190 after 8 days)
Archived data resolution	Same as model resolution	1.25 deg × 1.25 deg	1.0 deg × 1.0 deg
Perturbation method	Singular Vectors +Simplified Extended Kalman Filter	Singular Vectors + Local Ensemble. Transform Kalman Filter	Ensemble Kalman Filter
# of members	51	27	21

876
877